Multidimensional Ni-Co-sulfide heterojunction electrocatalyst for highly efficient overall water splitting

Wenxia Chen[1], Yingjie Hu[1,3], Peng Peng[2], Jinhai Cui[1], Junmei Wang[1], Wei Wei[1], Yongya Zhang[1], Kostya (Ken) Ostrikov[4] and Shuang-Quan Zang[2*]

ABSTRACT Heterostructure engineering holds exceptional promise for the development of high-performance electrocatalysts for overall water splitting. However, production of inexpensive and high-efficiency bifunctional electrocatalysts remains a challenge. Herein, we demonstrate a simple method to synthesize a paper-mulberry (*Broussonetia papyrifera*)-inspired $Co_9S_8@CoNi_2S_4$/nickel foam ($Co_9S_8@CoNi_2S_4$/NF) heterojunction with high catalytic activity and stability. The process involves *in situ* growth of NiCo layered double hydroxide and *in situ* derivatization of ZIF-67, followed by the S heteroatom doping. The $Co_9S_8@CoNi_2S_4$/NF benefits from the heterostructure and functional advantages of multidimensional building blocks including one-dimensional (1D) nanowires, 2D nanosheets and nanoparticles. The optimized $Co_9S_8@CoNi_2S_4$/NF heterojunction with 10% sulphur content reveals excellent electrocatalytic activity with the lower overpotentials of 68 mV for hydrogen evolution reaction (HER) and 170 mV for oxygen evolution reaction (OER) at 10 mA cm^{-2} in the 1.0 mol L^{-1} KOH solution, which is superior to the recently reported transition metal based electrocatalysts. The outstanding performance is attributed to the strong interface coupling between $CoNi_2S_4$ and Co_9S_8, the advantage of multidimensional structure and the customized electronic structure. The density functional theory suggests that the interface between Co_9S_8 and $CoNi_2S_4$ optimizes the adsorption of the multiple intermediates and further facilitates water splitting kinetics. This work offers a generic approach for heterostructure engineering design of high-performance catalytic system applications.

Keywords: heterojunction, heteroatom doping, multidimensional nanostructure, electrocatalysts, overall water splitting

INTRODUCTION

Since hydrogen fuels produce no carbon dioxide and have a high energy density, they are recognized as one of the most promising renewable energy sources for resolving the world's rising environmental pollution and energy deficit concerns. It is critical to rapidly develop cost-effective and efficient technologies for hydrogen generation in order to lessen our dependency on non-renewable fossil fuels [1–4]. Electrocatalysis is an efficient method for producing high purity hydrogen through the hydrogen evolution reaction (HER) and oxygen evolution reaction (OER) processes that occur during water electrolysis [5,6]. Precious metals and their oxides (such as Pt/C and RuO_2) are usually used as water splitting catalysts. Though their HER and OER performances are outstanding, they are rare and cost, and so ultimately fail to satisfy the requirements for scalable and economically viable hydrogen generation [7–10]. Therefore, designing and developing new low-cost, high-efficiency catalysts for water electrolysis to lower reaction over-potentials and increase energy conversion efficiency are desired.

Among the several possible electrode materials, layered double hydroxide (LDH) nano-sheets [11,12] have been extensively employed to synthesize transition metal sulfides such as W-S [13,14], Mo-S [15], and Ni-Co-S [16,17]. To regulate and improve the electrocatalytic activity of catalysts, morphological engineering and heterogeneous structure (heterostructure) engineering have been intensively pursued. Numerous synthetic techniques have been developed to improve electrocatalytic performance. For instance, Co-Fe-S@Prussian blue (PB) nanoboxes [18], Co-S-O/N,S-codoped carbon nanosheets (NSCN) [19], and NiS/MoO$_3$/nickel foam (NF) nanosheets/nanorods [20] exhibit potential electrocatalytic water splitting properties. An intriguing technique was purposed to rationally design hierarchical nanostructures as high-efficiency electrocatalysts. Apart from standard morphological tweaking, tailored heterostructures composed of transition-metal chalcogenides are worth exploration. Indeed, such heterostructures incorporate electronically linked interfaces which synergistically increase the effects of each element in the heterostructure. Numerous material systems have been investigated as heterostructured catalysts for enhanced electrochemical performance, including CoNi$_2$S$_4$@NiMn LDH/superhydrophilic carbon cloth (SCC) [21], MoS$_2$/Ni$_3$S$_2$ [22], FeNiCoS@Co$_3$O$_4$ NAs/NF [23], and CoS$_2$@MXene [24]. Nonetheless, the HER activity of transition metal sulfides is hindered by poor electron transport and low active site reactivity; metal sulfides' OER activity is far from

[1] School of Chemistry and Chemical Engineering, Henan Engineering Center of New Energy Battery Materials, Shangqiu Normal University, Shangqiu 476000, China
[2] Henan Key Laboratory of Crystalline Molecular Functional Materials, Henan International Joint Laboratory of Tumor Theranostical Cluster Materials, Green Catalysis Center and College of Chemistry, Zhengzhou University, Zhengzhou 450001, China
[3] Key Laboratory of Advanced Functional Materials of Nanjing, Nanjing Xiaozhuang University, Nanjing 211171, China
[4] School of Chemistry and Physics and Centre for Materials Science, Queensland University of Technology, Brisbane, QLD 4000, Australia
* Corresponding author (email: zangsqzg@zzu.edu.cn)

acceptable level. Thus, it is necessary to fabricate high-performance bi-functional heterostructured catalysts *via* morphology and heterojunction engineering in order to simultaneously modulate the electronic structure and active sites of the catalysts while optimizing the adsorption of the multiple intermediates in the HER and OER processes. Numerous heterostructured electrocatalysts with exceptional performance have been described using chemical doping, nanostructure engineering, and composite building methodologies to maximize the synergistic impact of the heterojunction structure, strain effect, and electron interaction. But few heterojunction catalysts have been created with high specific surface area, high conductivity, and optimized interface structure.

Herein, a three-dimensional (3D) $Co_9S_8@CoNi_2S_4/NF$ heterostructure resembling the flowering plants of paper mulberry (*Broussonetia papyrifera*) is designed using a surface reconstruction strategy involving a customized hydrothermal process and room-temperature growth, followed by sulfur atom doping (Scheme 1). The as-synthesized 3D $Co_9S_8@CoNi_2S_4/NF$ heterostructure electrode exhibits strong coupling between the $CoNi_2S_4$ and Co_9S_8 phases and integrates 1D nanowires with high ion/electron transport, 2D nanosheets with a large specific surface area, and 3D nickel foam with high electrical conductivity. The 3D $Co_9S_8@CoNi_2S_4/NF$ heterojunction catalyst demonstrates a remarkable electrocatalytic activity, with an overpotential of just 170 mV for OER and 68 mV for HER at 10 mA cm^{-2}, in a 1 mol L^{-1} KOH solution. According to density functional theory (DFT) calculations, the coupled interface between the Co_9S_8 and

$CoNi_2S_4$ phases improves the adsorption of numerous intermediates and increases the kinetics of water splitting, hence enhancing the electrocatalytic performance. Overall, this study establishes an experimental and theoretical foundation for the rational design and manufacture of heterostructured electrocatalysts with high catalytic activity and stability by targeted morphology and heterojunction engineering. As such, this strategy may contribute to the acceleration of the development of new functional materials for a variety of energy storage and conversion applications.

EXPERIMENTAL SECTION

Chemicals and reagents
Sigma-Aldrich Co., Ltd. provided 2-methylimidazole (2MeIm, $C_4H_6N_2$, 99.0%), urea, and thioacetamide. Sinopharm Group provided nickel nitrate hexahydrate (Ni(NO$_3$)$_2$·6H$_2$O) and cobalt nitrate hexahydrate (Co(NO$_3$)$_2$·6H$_2$O). Shanghai Maclean Biochemical Technology Co., Ltd. provided potassium hydroxide (KOH). All reagents were used without further purification.

Preparation of NiCo LDH/NF and NiCo LDH@ZIF-67/NF and ZIF-67/NF
The NF was cleaned with acetone, 1 mol L^{-1} HCl, and deionized water using ultrasonication for 10 min to remove surface oil stains. Then 2402 mg of urea, 1454 mg of Ni(NO$_3$)$_2$·6H$_2$O, 1455 mg of Co(NO$_3$)$_2$·6H$_2$O, and 40 mL of deionized water were mixed uniformly. The mixed solution was then placed to a
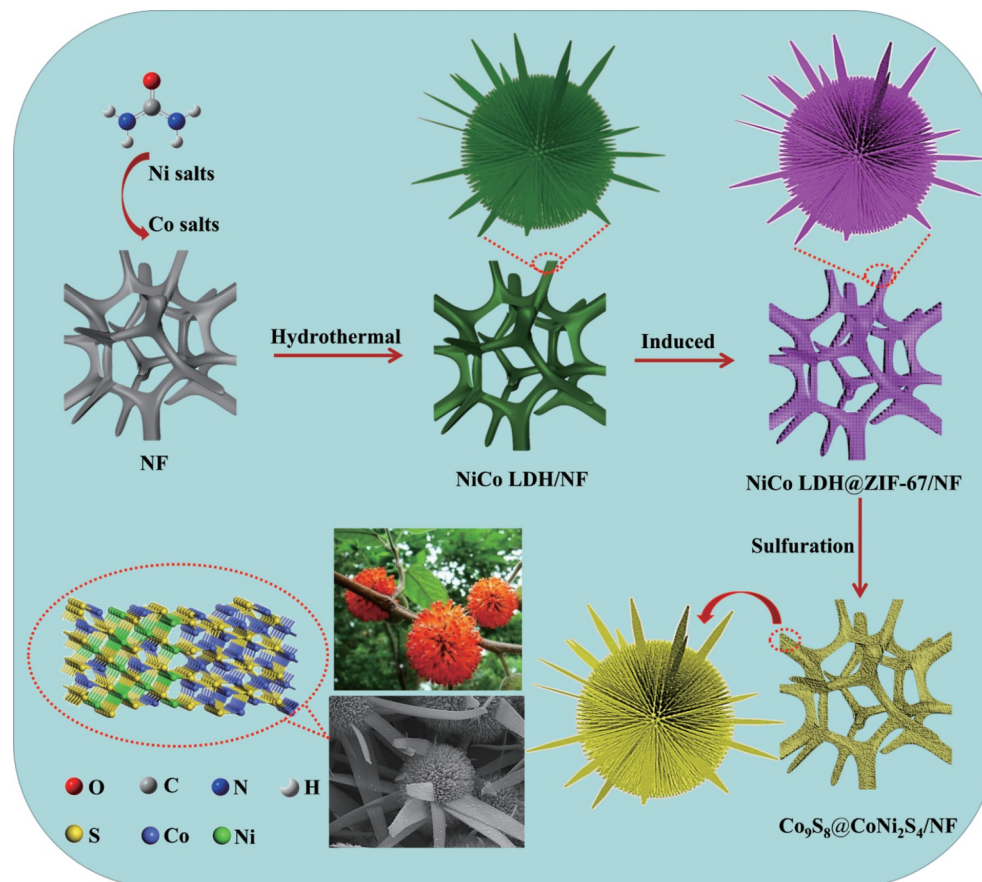
Scheme 1 The synthesis of 3D, multidimensional $Co_9S_8@CoNi_2S_4/NF$ heterostructured catalysts is inspired by the intricate 3D structure of a natural flowering paper mulberry.

50-mL sealed reactor and the cleaned NF was added. Following that, the autoclave was maintained at 130°C for 14 h. Washing and drying were used to get the NiCo LDH/NF. Similarly, by altering the Ni/Co molar ratio in the feed, Ni_1Co_9 LDH/NF, Ni_2Co_8 LDH/NF, and Ni_4Co_6 LDH/NF were prepared with the same procedure. Additionally, the NiCo LDH/NF precursors were produced at three different temperatures (120, 135 and 140°C) in order to optimize the catalytic performance.

To synthesize NiCo LDH@ZIF-67/NF, 25 mL of methanol solution containing 2MeIm (0.3 g) was prepared. Then, the prepared NiCo LDH/NF was added to the aforesaid solution for 5 h at room temperature, and the NiCo LDH@ZIF-67/NF was obtained. Similarly, by varying the precursor type, a variety of precursor derivatives were prepared, such as NiCo LDH@ZIF-67/NF-120, NiCo LDH@ZIF-67/NF-135, and NiCo LDH@ZIF-67/NF-140.

To prepare ZIF-67/NF, 1 mmol of $Co(NO_3)_2 \cdot 6H_2O$ and 4 mmol of 2MeIm were added to a menthol solution (25 mL), respectively. The aforesaid solution was then uniformly mixed, and NF was immersed for 24 h at room temperature. Then the precipitates of ZIF-67/NF were washed and dried.

Synthesis of $Co_9S_8@CoNi_2S_4$/NF, Co_9S_8/NF and $CoNi_2S_4$/NF

The sulfur powder was added to the top stream of a tubular furnace, and NiCo LDH@ZIF-67/NF, ZIF-67/NF and NiCo LDH/NF were respectively placed downstream of the tube furnace calcined at 350°C for 2 h in the presence of nitrogen gas. The sulfur powder and NiCo LDH@ZIF-67/NF were fed in at a mass ratio of 10%, and the resulting product was labeled as $Co_9S_8@CoNi_2S_4$/NF, Co_9S_8/NF, and $CoNi_2S_4$/NF. Similarly, when the sulfur powder and the NiCo LDH@ZIF-67/NF feeding mass ratios were 5%, 7%, and 12%, respectively, a series of $Co_9S_8@CoNi_2S_4$/NF heterojunction catalysts with varying sulfur contents were produced. The catalysts synthesized in this manner are designated as 5% $Co_9S_8@CoNi_2S_4$/NF, 7% $Co_9S_8@CoNi_2S_4$/NF, and 12% $Co_9S_8@CoNi_2S_4$/NF.

Additionally, the precursor derivatives NiCo LDH@ZIF-67/NF-120, NiCo LDH@ZIF-67/NF-135 and NiCo LDH@ZIF-67/NF-140 were further sulphated. The feed mass ratio of the sulfur powder and these precursor derivatives were 10%, yielding $Co_9S_8@CoNi_2S_4$/NF-120, $Co_9S_8@CoNi_2S_4$/NF-135 and $Co_9S_8@CoNi_2S_4$/NF-140.

Characterizations

X-ray diffraction (XRD) was performed using a Rigaku Ultima IV X-ray diffractometer. The N_2 adsorption/desorption isotherms were utilized to determine the specific surface area and pore structure at 77 K. (Belsorp-max). Scanning electron microscopy (SEM, JEOL, Japan) and transmission electron microscopy (TEM, JEM-2010, Japan) were used to examine the morphologies and the microstructures of the samples. The elemental chemical states of the catalyst materials were determined using X-ray photoelectron spectroscopy (XPS, VG Scientific).

Electrochemical analyses

The electrochemical water splitting experiment was conducted in a KOH solution (1 mol L^{-1}, pH = 14) with an electrochemical workstation (model CHI660E) equipped with a three-electrode setup. The counter electrode was a carbon rod, and the reference electrode was a Hg/HgO (saturated KCl) electrode. The working electrodes were CoNi LDH/NF, CoNi LDH@ZIF-67/NF, and

$Co_9S_8@CoNi_2S_4$/NF, respectively. The linear sweep voltammetry (LSV) was conducted at a scan rate of 5 mV s^{-1}. Electrochemical impedance spectroscopy (EIS) measurements were performed between 100 kHz and 0.1 Hz. Based on the Nernst equation, all potentials were converted to reversible hydrogen electrodes (RHE):
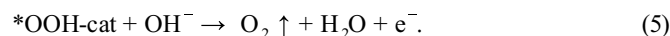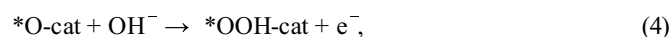
$$E_{(RHE)} = E_{(Hg/HgO)} + 0.095 + 0.059 \text{ pH}. \quad (1)$$

Besides, the overpotential of the OER was calculated by subtracting the equilibrium potential of OER with the actual measured potential value. Additionally, the electrochemical active surface area (ECSA) is another essential parameter used to compare different electrocatalysts' activity, as the kinetics of the HER over electrocatalysts is directly linked to their ECSA. Being directly related to ECSA, double layer capacitance (C_{dl}) was determined from cyclic voltammetry (CV) measurements with scan rates ranging from 20 to 100 mV s^{-1}.

DFT calculations

All calculations were carried out using the scheme of spin-polarized DFT with the Cambridge Sequential Total Energy package (CASTEP). To be precise, the exchange-correlation energy was described using the Perdew-Burke-Ernzerhof (PBE) exchange-correlation functional inside the generalized gradient approximation, with a plane-wave cutoff energy of 450 eV. Grimme's semi-empirical DFT-D was used in the calculations to ensure a more accurate representation of the electron interaction over a large distance. Tolerances for geometric convergence were established at 0.03 eV $Å^{-1}$, 10^{-5} eV $atom^{-1}$ for maximum force, 0.001 Å for maximum displacement, and 0.5 GPa for maximum stress. The sampling in the Brillouin zone was set with 3×3×1 by the Monkhorst-Pack method.

The OER route was defined as the sequential adsorption of intermediate species on the catalyst, with the following reaction energies:

$$OH^- + cat \rightarrow *OH\text{-}cat + e^-, \quad (2)$$

$$*OH\text{-}cat + OH^- \rightarrow *O\text{-}cat + H_2O + e^-, \quad (3)$$

$$*O\text{-}cat + OH^- \rightarrow *OOH\text{-}cat + e^-, \quad (4)$$

$$*OOH\text{-}cat + OH^- \rightarrow O_2 \uparrow + H_2O + e^-. \quad (5)$$

The "cat" symbolized the active site when OER occurred. The "*OH", "*O", "*OOH" symbols denoted the adsorbed intermediate species on the active sites. To determine the OER activity, we used the computational standard hydrogen electrode model to calculate the free energy ($\Delta G_1 - \Delta G_4$):

$$\Delta G_1 = G_{OH\text{-}cat} - G_{cat} - G_{H_2O} + G_{H_2}/2 - eU + K_B T \ln 10 \times \text{pH}, \quad (6)$$

$$\Delta G_2 = G_{O\text{-}cat} - G_{OH\text{-}cat} + G_{H_2}/2 - eU + K_B T \ln 10 \times \text{pH}, \quad (7)$$

$$\Delta G_3 = G_{OOH\text{-}cat} - G_{O\text{-}cat} - G_{H_2O} + G_{H_2}/2 - eU + K_B T \ln 10 \times \text{pH}, \quad (8)$$

$$\Delta G_4 = 4.92 - \Delta G_1 - \Delta G_2 - \Delta G_3. \quad (9)$$

$-eU$ denotes the free energy changes associated with a single electron transfer, U is the electrode potential in relation to the standard hydrogen electrode, K_B is the Boltzmann constant and T is the temperature. For pH $\neq$ 0, the effect of pH on free energy

could be described as $-K_BT\ln 10 \times$ pH.

The Gibbs free energy change (ΔG_H) for HER is as follows: $\Delta G_{H*} = \Delta E_{H*} + \Delta E_{ZPE} - T\Delta S$, where ΔE_{H*}, ΔE_{ZPE} and ΔS are the adsorption energy of atomic hydrogen on the given surface, zero point energy correction and entropy change of H* adsorption, respectively. The value of ΔE_{H*} is calculated as $\Delta E_{H*} = E_{tot} - E_{sub} - E_{H_2}/2$, where E_{tot} and E_{sub} are the energies of H absorbed systems and the clean given surface, respectively, and E_{H_2} is the energy of molecular H_2 in the gas phase.

RESULTS AND DISCUSSION

Materials characterization

Multiple sophisticated microscopy and spectroscopic methods were used to characterize the resultant $Co_9S_8@CoNi_2S_4$/NF heterostructures. To determine the optimal Ni/Co feed ratio in the precursor, a series of test catalysts with varying Ni/Co ratios were constructed. When the Ni/Co molar ratio was 1:9, the NiCo LDH/NF sample is composed of 3D microspheres formed from 1D nanowires, as seen in Fig. S1a. By raising the Ni/Co molar ratio to 2:8, the NiCo LDH/NF sample keeps its 3D microsphere structure joined with 1D nanowires (see Fig. S1b), which grow in nanometre size as the Ni concentration increases. As shown in Fig. S1c, when the Ni/Co molar ratio is 4:6, the 3D NiCo LDH/NF microspheres are still built using 1D nanowires, and their diameter increases as the Ni/Co molar ratio increases. Additionally, as shown in the inset of Fig. S1c, the enlarged SEM

images suggest that the 1D nanowires are linked and tend to convert into nanosheets. By changing the Ni/Co molar ratio to 5:5, the 3D NiCo LDH/NF flower-shaped structure perfectly combined the 1D nanowires representing the stamens of the flower and the 2D nanosheet-like petals are disclosed in Fig. S1d. These findings demonstrate that the morphologies of the NiCo LDH/NF samples vary according to the Ni/Co molar ratios used, and nanosheets and nanowires can coexist when the nickel to cobalt ratio is just perfect. To be more precise, a portion of the Ni element and N in urea combine to produce urease, which may accelerate the hydrolysis of urea into ammonia and carbon dioxide. This is primarily because part of the interconnected nanowires will be separated during the gas release process, and the remaining interconnected nanowires will tend to change into nanosheets. To study the effect of multi-dimensional materials for electrocatalytic performance and further enhance catalytic activity, *in situ* derived MOF particles and sulfur atom doping were located on the NiCo LDH/NF precursor with a Ni/Co ratio of 5:5 to further regulate its electronic structure and obtain multidimensional highly efficient chalcogenide as a difunctional electrocatalyst.

As seen in Fig. 1a, b, the as-prepared multidimensional $Co_9S_8@CoNi_2S_4$/NF heterojunction is constituted of 1D nanowires, 2D nanosheets, and nanoparticles, and the morphological is similar to its precursor NiCo LDH@ZIF-67/NF (Fig. S2). The SEM micrographs demonstrate an uncanny resemblance between the $Co_9S_8@CoNi_2S_4$/NF morphology and the 3D

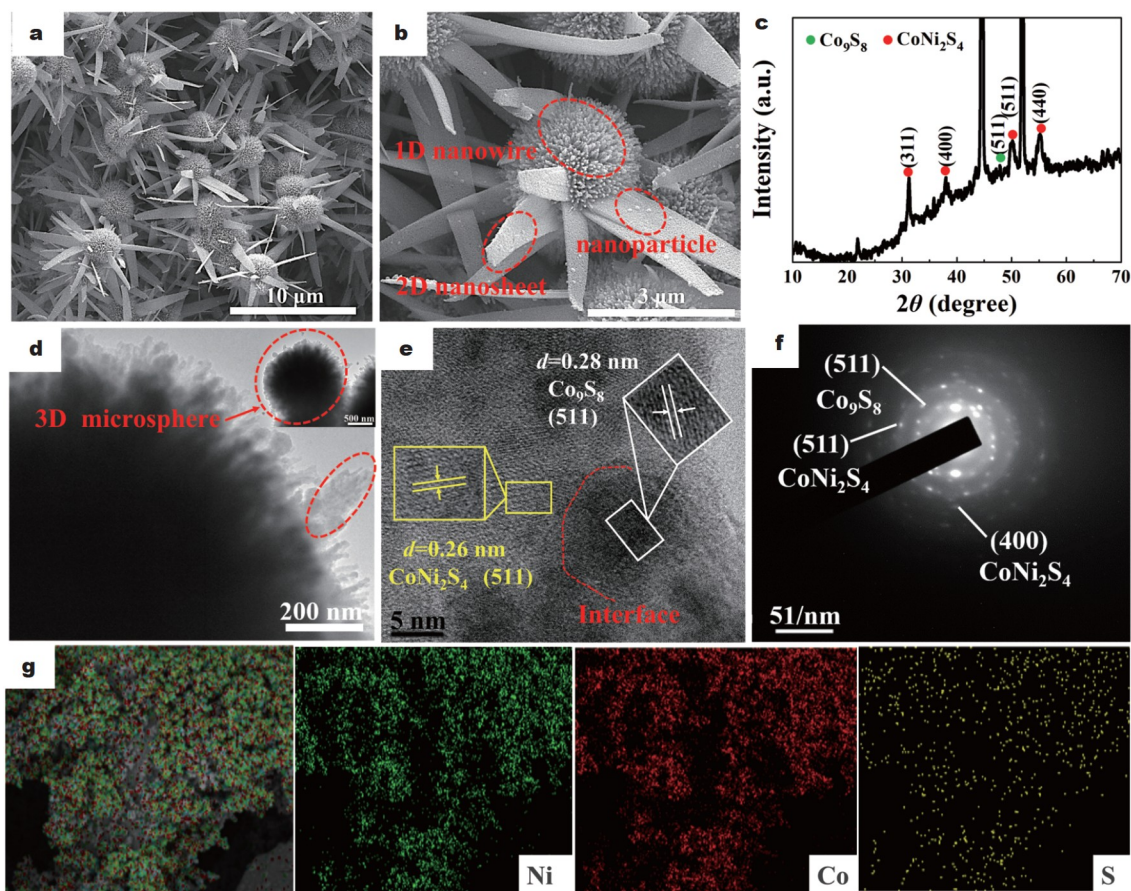**Figure 1** Multidimensional $Co_9S_8@CoNi_2S_4$/NF heterostructures and their microstructural features. (a, b) SEM images, (c) XRD pattern, (d) TEM, (e) HRTEM images, (f) the corresponding SAED pattern, and (g) the SEM elemental mapping images of the $Co_9S_8@CoNi_2S_4$/NF.

structure of paper mulberry during the blossoming season (Scheme 1). For comparison, the morphology of Co_9S_8/NF and $CoNi_2S_4$/NF was studied. As illustrated in Fig. S3, the Co_9S_8/NF has a polyhedral structure, whereas $CoNi_2S_4$/NF preserves the 3D floral structure formed by nanowires and nanosheets as illustrated in Fig. S4.

Furthermore, the crystal structures of the $Co_9S_8@CoNi_2S_4$/NF heterojunction was analyzed using XRD as shown in Fig. 1c. The peaks located at 31.5°, 38.4°, 50.3° and 55.1° are indexed to the (311), (400), (511), and (440) crystal planes of the cubic $CoNi_2S_4$ (JCPDS No. 24-0334) [25]. In addition, the peak at 47.6° corresponds to the (511) plane of Co_9S_8 [26,27]. As shown in Fig. 1d and the inset, the 3D $Co_9S_8@CoNi_2S_4$/NF is constituted of nanoparticles, 1D nanowires, and 2D nanosheets like the paper mulberry, which is consistent with the SEM results. The high-resolution TEM (HRTEM) image (Fig. 1e) demonstrates the heterojunctions with well-resolved lattice fringes, revealing the Co_9S_8 (511) (0.28 nm) and $CoNi_2S_4$ (511) (0.26 nm) phases. As shown in Fig. 1f, the selected area electron diffraction (SAED) pattern demonstrates the presence of the (440) and (511) diffraction planes in $CoNi_2S_4$ and Co_9S_8, which agrees well with the XRD results. Moreover, Fig. 1g depicts the SEM-based low-

resolution elemental mapping of the $Co_9S_8@CoNi_2S_4$/NF heterojunction catalyst, demonstrating the homogenous distribution of Co, Ni, and S elements.

XPS measurements were used to determine the chemical composition and elemental state of $Co_9S_8@CoNi_2S_4$/NF. The survey spectrum of the $Co_9S_8@CoNi_2S_4$/NF heterojunction is shown in Fig. 2a, revealing the Ni 2p, Co 2p, and S 2p peaks. As seen in Fig. 2b, the high-resolution spectrum of Ni 2p reveals two primary peaks at 856.3 and 874.0 eV, corresponding to the Ni $2p_{3/2}$ and Ni $2p_{1/2}$ states, respectively, accompanied by satellite peaks at 861.8 and 880.1 eV [28–30]. In the high-resolution Co 2p spectrum (Fig. 2c), the two primary peaks centered at 781.4 and 797.1 eV, are ascribed to the spin-orbit splitting of Co $2p_{3/2}$ and Co $2p_{1/2}$ states, which is compatible with the existence of Co^{2+} and Co^{3+} species [31,32]. The peak at 776.0 eV is attributed to the presence of Co^{3+} ions. As shown in Fig. 2d, the S 2p spectrum exhibits peaks at 162.4 and 163.5 eV, corresponding to the S $2p_{3/2}$ and S $2p_{1/2}$ binding energies, respectively. These states are caused by the S_2^{2-} exposed on the metal-sulfur sites in Co_9S_8, indicating the formation of the Co_9S_8 phase in the $Co_9S_8@CoNi_2S_4$/NF heterojunction catalyst [33,34]. The peak at 168.5 eV well matches the highly charged state S^{4+} on the edge of
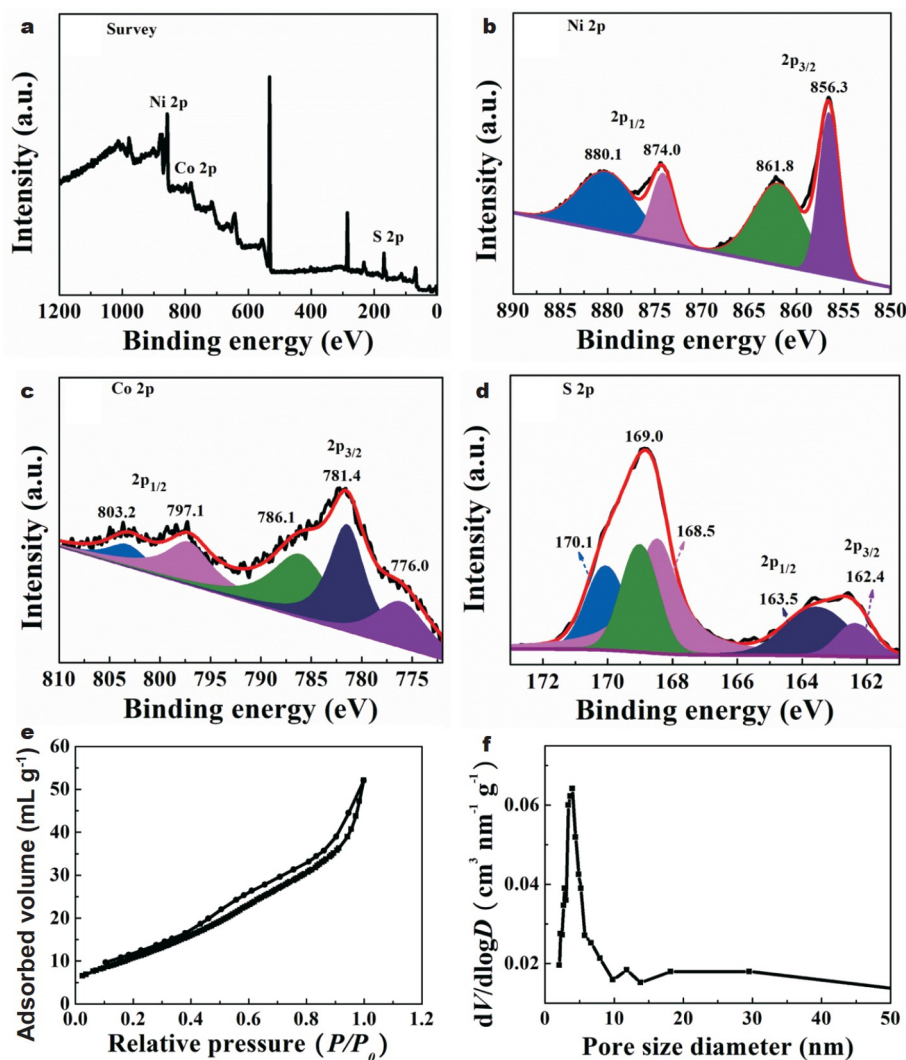

Figure 2 Elemental bonding states and porous structure of the catalysts. XPS spectra of (a) survey, (b) Ni 2p, (c) Co 2p, and (d) S 2p regions of $Co_9S_8@CoNi_2S_4$/NF. (e) The N_2 adsorption/desorption isotherms and (f) pore size distribution of $Co_9S_8@CoNi_2S_4$/NF.

$CoNi_2S_4$.

The specific area and pore size distribution of the multidimensional $Co_9S_8@CoNi_2S_4$/NF heterojunction catalyst were further analyzed using the Brunauer-Emmett-Teller (BET) method. According to Fig. 2e, the integrated multidimensional $Co_9S_8@CoNi_2S_4$/NF heterojunction has a high specific surface area of 42.80 m^2 g^{-1}, which is larger than that of the NiCo LDH material (13.76 m^2 g^{-1}) in Fig. S5. Besides, the pore size distribution of $Co_9S_8@CoNi_2S_4$/NF is centered at 5–7 nm, as shown in Fig. 2f, indicating the material's persistent mesoporous structure. The increased surface area and abundant mesoporous structure endow the multidimensional $Co_9S_8@CoNi_2S_4$/NF heterojunction with a higher mass loading on the catalytically active exposed surface, which is convenient for the electrolytes, further enhancing the electrocatalytic activity.

Electrocatalytic performance

The electrocatalytic HER performance was evaluated in 1.0 mol L^{-1} KOH aqueous solution. As shown in Fig. 3a and Fig. S6, freshly prepared $Co_9S_8@CoNi_2S_4$/NF heterojunction catalyst has a lower HER overpotential of 68 mV to achieve a current density of 10 mA cm^{-2}, which is much lower than that

for NiCo LDH/NF (181 mV), NiCo LDH@ZIF-67/NF (152 mV), Co_9S_8/NF (224 mV), $CoNi_2S_4$/NF (119 mV) and recently reported transition metal-based composites (Table S1), and close to that of the commercial Pt/C/NF (36 mV). The result indicates that the synergistic effect of Co_9S_8 and $CoNi_2S_4$ results in an increase in catalytic activity during the HER process. Additionally, the effect of temperature on the catalyst precursors has been established (see Fig. S7), and it has been demonstrated that the $Co_9S_8@CoNi_2S_4$/NF heterojunction exhibits the best catalytic activity at 130°C when compared with other temperatures. Furthermore, to further investigate the influence of sulfurization concentration on the hydrogen evolution performance of the catalyst, the $Co_9S_8@CoNi_2S_4$/NF heterojunction catalyst was synthesized with different sulfur contents, namely 5%, 7%, 10%, and 12%. As seen in Fig. S8, the activity of the $Co_9S_8@CoNi_2S_4$/NF heterojunction increases with the increase of S content. When the sulfur concentration of $Co_9S_8@CoNi_2S_4$/NF reaches 10%, it exhibits the maximum HER activity. The activity of the $Co_9S_8@CoNi_2S_4$/NF catalyst diminishes when the S content continues to increase (12%), which may be due to the more pronounced porosity structure created by the incorporation of sulfur particles. It hinders the complete contact between the
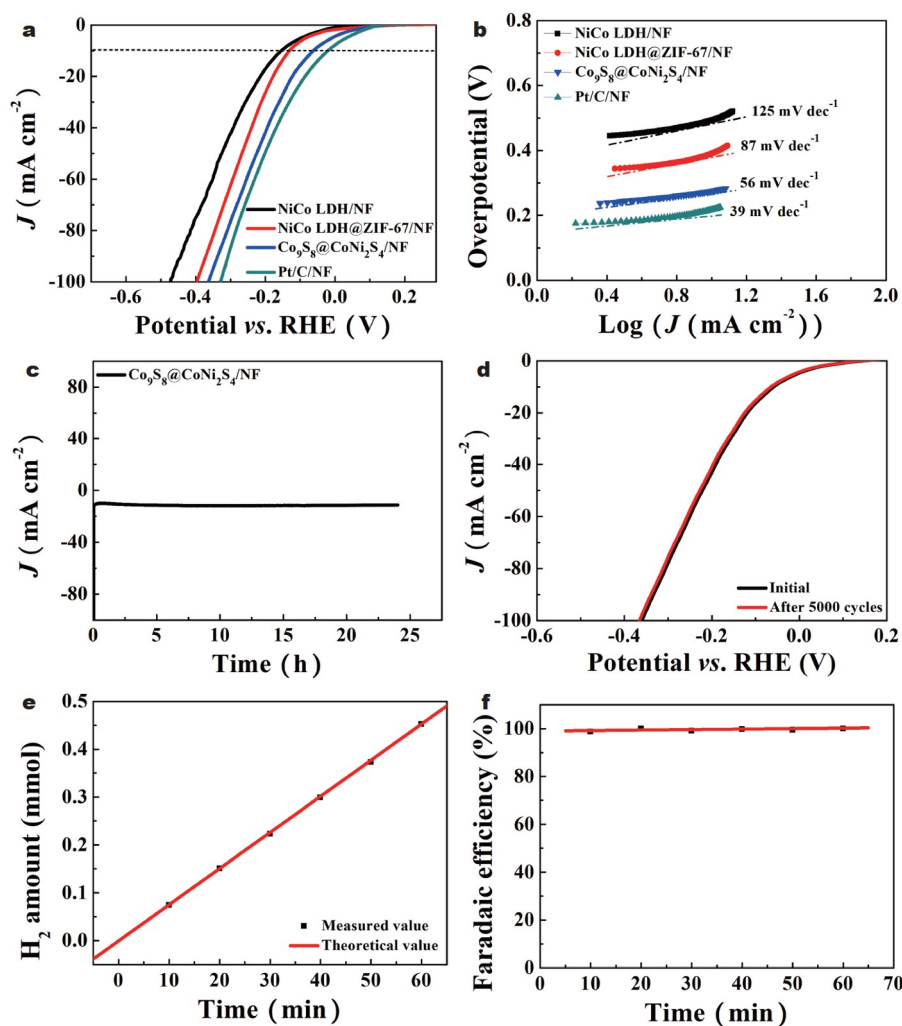

Figure 3 HER performance of the $Co_9S_8@CoNi_2S_4$/NF catalyst. (a) Polarization curves, (b) Tafel slopes, (c) the chronoamperometric curve of $Co_9S_8@CoNi_2S_4$/NF at 10 mA cm^{-2}, (d) the polarization curve of $Co_9S_8@CoNi_2S_4$/NF before and after 5000 cycles, (e) the H_2 generation of $Co_9S_8@CoNi_2S_4$/NF driven with 10 mA cm^{-2}, and (f) the corresponding FE.

electrolyte and the catalyst, and results in decreased mass transfer and catalytic activity. Besides, the observed Tafel slope of $Co_9S_8@CoNi_2S_4$/NF is 56 mV dec^{-1}, which is lower than the values for NiCo LDH/NF (125 mV dec^{-1}), and NiCo LDH@ZIF-67/NF (87 mV dec^{-1}), and approaches to that of Pt/C (39 mV de^{-1}) in Fig. 3b. The finding indicates that the $Co_9S_8@CoNi_2S_4$/NF heterojunction has a higher reaction rate than its counterparts. Long-term stability is a critical factor in determining the performance of catalysts. As demonstrated in Fig. 3c, the current density at 10 mA cm^{-2} nearly remains constant after 24 h, demonstrating that the $Co_9S_8@CoNi_2S_4$/NF heterostructure has outstanding endurance. Furthermore, only a negligible variation was found from the CV curve after 5000 cycles in Fig. 3d. These results manifest the exceptional long-term HER stability of the electrocatalysts based on $Co_9S_8@CoNi_2S_4$/NF heterostructures.

Subsequently, the charge transfer kinetics of HER was investigated using EIS. Fig. S9 illustrates the impedance spectra. The lowest charge transfer resistance (R_{ct}) in the $Co_9S_8@CoNi_2S_4$/NF (10.0 Ω) heterojunction suggests an increased charge transfer rate, which is beneficial to the HER. The difference in R_{ct} for these catalysts clearly indicates that S doping can promote the redistribution of S, Ni, and Co atoms and surface reconstruction inside the catalyst, resulting in enhanced reaction kinetics and HER activity.

To investigate the catalyst's efficiency, the hydrogen production rate of the $Co_9S_8@CoNi_2S_4$/NF heterojunction was determined (Fig. 3e). The H$_2$ production rate is around 0.452 mmol h^{-1}, which is higher than that of recent publications on transition metal-based composites such as (FeCoNi)$_9$S$_8$-MoS$_2$ (0.370 mmol h^{-1}) [35], Co$_{0.13}$Ni$_{0.87}$Se$_2$/Ti (0.330 mmol h^{-1} [36], hierarchical whisker-on-sheet (HWS) NiCoP (0.180 mmol h^{-1} cm^{-2}) [37], and core/shell Ni/NiCoP (0.160 mmol h^{-1} cm^{-2}) [38]. The superior hydrogen generation rate of the $Co_9S_8@CoNi_2S_4$/NF heterojunction is primarily attributed to the heterostructure composed of coupled CoNi$_2$S$_4$ and Co$_9$S$_8$ phases, multidimensional structural and functional features, exposed high-density active sites, and a customized electronic structure. As shown in Fig. 3f, the experimental results are nearly consistent with the predicted H$_2$ value, indicating that the Faradaic efficiency (FE) of hydrogen evolution approaches 100%.

The morphology structure and chemical states of the catalysts were further analyzed after the HER. TEM image (Fig. S10) confirms that the morphology of the $Co_9S_8@CoNi_2S_4$/NF heterostructure remains unchanged. Additionally, the SEM mapping indicates that the Co, Ni, and S elements are uniformly distributed on the catalyst surface in Fig. S11. The XPS results for the $Co_9S_8@CoNi_2S_4$/NF after the HER are displayed in Fig. S12. In Fig. S12a, b, there is essentially little change in the Ni 2p and Co 2p spectra. Additionally, the O 1s spectrum exhibits peaks at 531.2 and 532.7 eV, which correspond to the surface-adsorbed OH$^-$ and water molecules (H$_2$O) (Fig. S12c) [39]. As shown in Fig. S12d, these peaks in the S 2p spectrum vary little after the HER process. Therefore, our findings indicate that the $Co_9S_8@CoNi_2S_4$/NF heterostructure undergoes essentially no phase transitions during the HER process.

Furthermore, the OER performance of the as-prepared catalysts was evaluated under the same conditions. Fig. 4a shows the polarization curves for the NiCo LDH/NF, NiCo LDH@ZIF-67/NF, $Co_9S_8@CoNi_2S_4$/NF, and commercial RuO$_2$/NF electrodes,

with corresponding overpotentials of 360, 320, 170, and 260 mV at 10 mA cm^{-2}. Clearly, the catalytic activity of the $Co_9S_8@CoNi_2S_4$/NF complex is higher than that of the Co$_9$S$_8$/NF and CoNi$_2$S$_4$/NF in Fig. S13, demonstrating the synergistic impact of Co$_9$S$_8$/NF and CoNi$_2$S$_4$/NF. The $Co_9S_8@CoNi_2S_4$/NF heterojunction composite possesses the competitive OER electrocatalytic activity, compared with the commercial RuO$_2$/NF catalyst and previously reported transition metal-based composites (Table S1), implying that the $Co_9S_8@CoNi_2S_4$/NF with abundant surface reactive sites has strong catalytic capacity toward OER. Furthermore, it can be observed that the optimized $Co_9S_8@CoNi_2S_4$/NF heterojunction displays the best OER electrocatalytic activity and the lowest overpotential compared with its counterparts (Figs S14, S15). Moreover, the Tafel slopes of the catalysts were calculated to quantify the OER kinetics of electrocatalysts. The obtained Tafel slope of the $Co_9S_8@CoNi_2S_4$/NF heterojunction catalyst is approximately 42 mV dec^{-1} as displayed in Fig. 4b. This value is much smaller than that of NiCo LDH/NF (139 mV dec^{-1}), NiCo LDH@ZIF-67/NF (95 mV dec^{-1}) and RuO$_2$/NF (61 mV dec^{-1}). In addition, the EIS values were measured to study the charge transfer kinetics for OER in Fig. S16. The EIS of the $Co_9S_8@CoNi_2S_4$/NF heterojunction is about 29 Ω, which is smaller than that of NiCo LDH/NF (36 Ω) and NiCo LDH@ZIF-67/NF (48 Ω), indicating that the OER process is facilitated. Moreover, the $Co_9S_8@CoNi_2S_4$/NF electrode demonstrates outstanding stability over a 24-h OER process in Fig. 4c. The polarization curves almost overlap after 5000 cycles (Fig. 4d), suggesting the excellent stability of the synthesized $Co_9S_8@CoNi_2S_4$/NF heterojunction electrocatalyst. Fig. 4e displays the produced O$_2$ amount of the $Co_9S_8@CoNi_2S_4$/NF catalyst. The O$_2$ production rate is about 0.225 mmol h^{-1}, which is better than the reported transition metal composites, for example, GDs/Co$_{0.8}$Ni$_{0.2}$P (100 μmol h^{-1}) [40], Cu/NiFe LDH (80 μmol h^{-1}) [41], and NiCoP NR@NS (0.09 mmol h^{-1} cm^{-2}) [42]. The coupling interface between Co$_9$S$_8$ and CoNi$_2$S$_4$ endows the multidimensional $Co_9S_8@CoNi_2S_4$/NF heterojunction catalyst with higher O$_2$ production rates, which can optimize the adsorption of multiple intermediates and further facilitate water splitting kinetics as validated by the DFT results. As seen in Fig. 4f, the measured O$_2$ concentration matches the predicted value, implying a nearly 100% FE for the OER process.

Moreover, the morphological and chemical states of the $Co_9S_8@CoNi_2S_4$/NF after the OER process were studied. As evidenced by the TEM investigation displayed in Fig. S17, the surface topography of $Co_9S_8@CoNi_2S_4$/NF stays nearly unaltered. As shown in Fig. S18, the SEM mapping indicates that the Co, Ni, and S components are still uniformly distributed across the $Co_9S_8@CoNi_2S_4$/NF surface. Additionally, XPS was used to examine any chemical composition differences. As shown in Fig. S19a, there is a negative shift in the valence state of Ni 2p between 857.7 and 874.8 eV due to the changes in the valence states of the constituents. In addition, the signal at 856.0 eV verifies the oxidation of the metal and the Ni–O bond, which is consistent with previous report [43]. The signal at 781.2 eV in the Co 2p spectrum in Fig. S19b indicates the existence of cobalt oxide species [44]. This finding demonstrates that the surface of the $Co_9S_8@CoNi_2S_4$/NF is oxidized during the OER process to create Ni/Co oxides or hydroxide. Moreover, the on-surface NiCoO/NiCoOOH species are expected to operate as OER catalysts, which is consistent with prior study of oxidative activation mediated by surface reconstruction in OER catalysts [45].
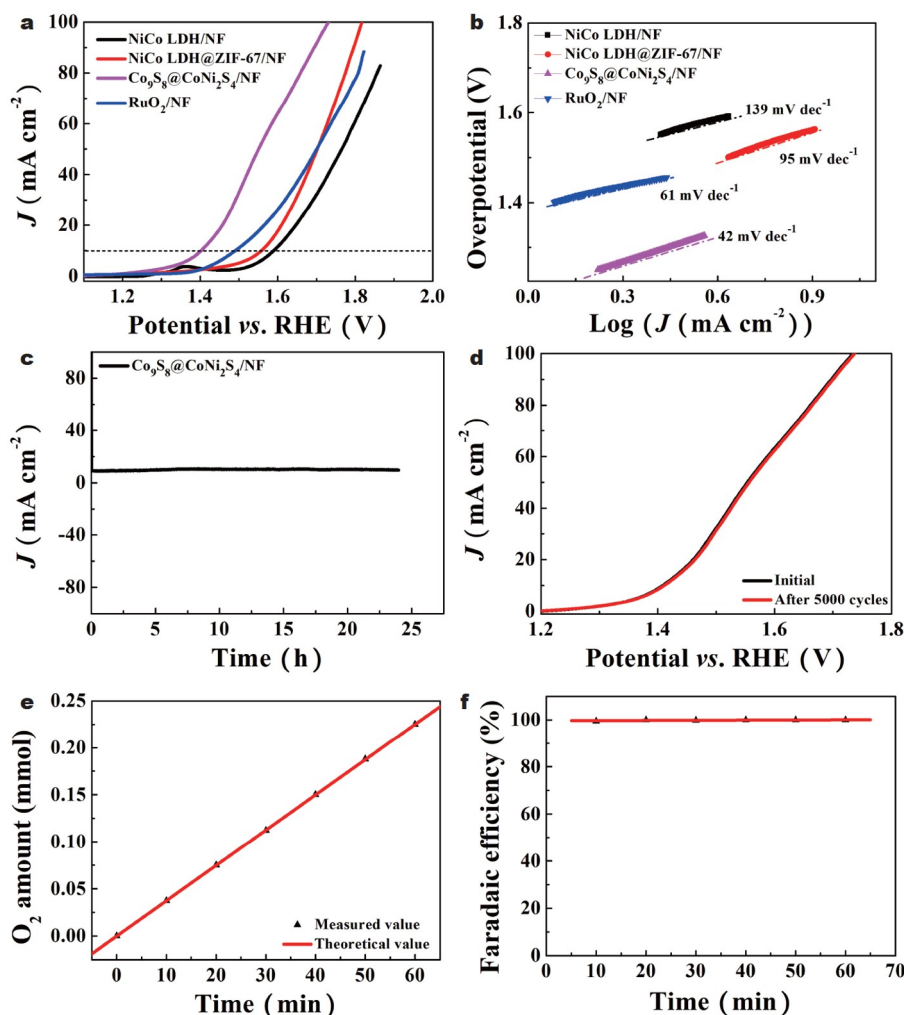
Figure 4 OER performance of the $Co_9S_8@CoNi_2S_4/NF$ catalyst. (a) Polarization curves, (b) Tafel slopes, (c) the chronoamperometric curve of $Co_9S_8@CoNi_2S_4/NF$ at 10 mA cm^{-2}, (d) the polarization curve of $Co_9S_8@CoNi_2S_4/NF$ before and after 5000 cycles, (e) the O_2 generation of $Co_9S_8@CoNi_2S_4/NF$ driven with 10 mA cm^{-2}, and (f) the corresponding FE.

As displayed in Fig. S19c, the peak at 530.8 eV in the O 1s spectrum is attributed to metal-oxygen bonding, indicating that the $Co_9S_8@CoNi_2S_4/NF$ heterostructures are indeed oxidized, resulting in fast electron transfer and thereby speeding the OER process. The signal at 169.6 eV in Fig. S19d corresponds to oxidized sulfur species, indicating that the catalyst was oxidized during OER, consistent with the results stated before.

Furthermore, the intrinsic activity of $Co_9S_8@CoNi_2S_4/NF$ was determined by its ECSA. Due to the fact that the ECSA is proportional to the double layer capacitance (C_{dl}), the C_{dl} is calculated using the CV curves to determine the ECSA. The CV curves collected at different scan rates ranging from 20 to 100 mV s^{-1} are shown in Fig. S20, demonstrating a linear connection between the current density and the scan rate. The calculated C_{dl} values of NiCo LDH/NF, NiCo LDH@ZIF-67/NF and $Co_9S_8@CoNi_2S_4/NF$ are 2.7, 4.2 and 33.9 mF cm^{-2}, respectively. The C_{dl} of $Co_9S_8@CoNi_2S_4/NF$ is substantially increased as compared with NiCo LDH/NF and NiCo LDH@ZIF-67/NF. In other words, the ECSA of the multidimensional $Co_9S_8@CoNi_2S_4/NF$ heterojunction is 12.5 and 8.1 times higher than that of the NiCo LDH/NF and NiCo LDH@ZIF-67/NF samples, respectively. Therefore, the $Co_9S_8@CoNi_2S_4/NF$ heterostructure deli-

vers the optimal catalytical surface area offering highly exposed catalytic active sites, which can be primarily ascribed to the multidimensional and heterojunction structure. Hence, the high ECSA of the multidimensional $Co_9S_8@CoNi_2S_4/NF$ heterojunction featuring plentiful active sites leads to the excellent electrocatalytic performance for both HER and OER half-reactions of water electrolysis.

The above results testify that the $Co_9S_8@CoNi_2S_4/NF$ heterojunction exhibits excellent HER and OER performance in terms of the catalytic activity and stability. As a consequence, the total water splitting performance of the $Co_9S_8@CoNi_2S_4/NF$ heterojunction catalyst was examined in a two-electrode electrolyzer device, as shown in Fig. 5a. Remarkably, the $Co_9S_8@CoNi_2S_4/NF$ heterojunction electrodes show the cell voltage of 1.49 V, which is lower than that of the NF substrate and previously reported transition metal-based electrodes (Table S2), demonstrating the significant electrocatalytic activity. In addition, the $Co_9S_8@CoNi_2S_4/NF$ heterojunction demonstrates good long-term stability when operated continuously for 24 h (Fig. 5b), as indicated by the $Co_9S_8@CoNi_2S_4/NF$ catalyst's stable current density of 10 mA cm^{-2} exhibiting minor variations. Furthermore, the entire water splitting system's hydrogen and oxygen production
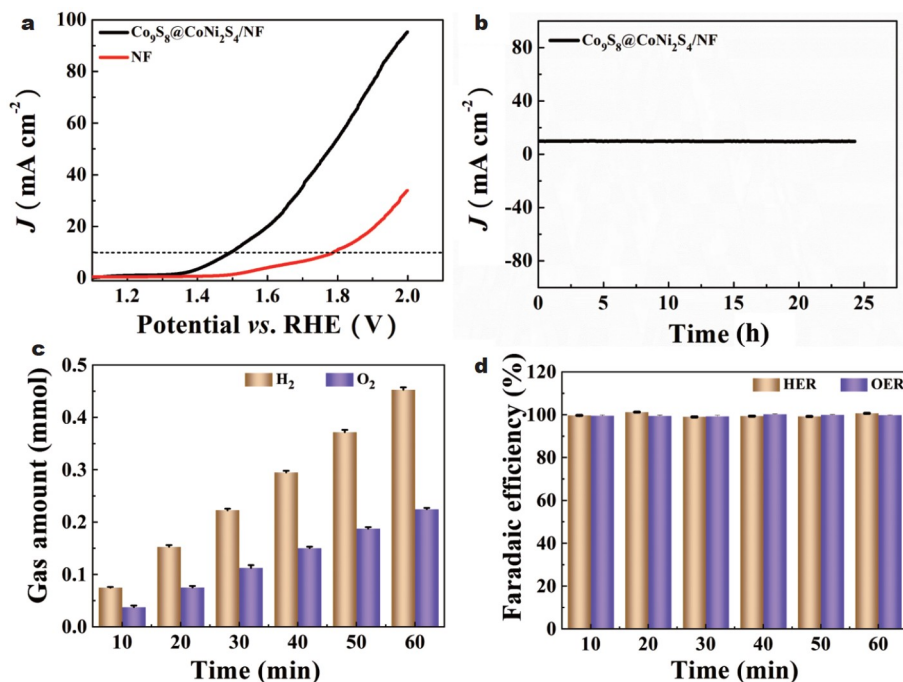
Figure 5 Performance of $Co_9S_8@CoNi_2S_4/NF$ heterostructures as a bifunctional water splitting electrocatalyst. (a) Overall water-splitting performance of $Co_9S_8@CoNi_2S_4/NF$ and blank NF in a two-electrode system, (b) time-dependent current density curve at 10 mA cm^{-2} for $Co_9S_8@CoNi_2S_4/NF$ in a two-electrode system, (c) H_2 and O_2 gas amounts as a function of water splitting time for $Co_9S_8@CoNi_2S_4/NF$ with error bars and (d) the corresponding FEs with error bars.

efficiencies were tested based on $Co_9S_8@CoNi_2S_4/NF$. As seen in Fig. 5c, the ratio of amounts of the produced H_2 and O_2 is close to 2:1, which corresponds to the theoretically estimated value. In other words, the HER and OER have achieved approximately 100% FE in the whole water splitting process, as seen in Fig. 5d.

Catalytic mechanisms by *ab-initio* atomistic simulations
To acquire a better understanding of the heterointerface influence on the HER and OER performance of the $Co_9S_8@CoNi_2S_4/NF$ structure, we used DFT to calculate energy changes and gain insight into the catalytic process at the generated heterointerfaces. Fig. S21 and Fig. 6a show the optimized Co_9S_8, $CoNi_2S_4$ and $Co_9S_8@CoNi_2S_4$ atomistic models. The $Co_9S_8@CoNi_2S_4$ heterojunction catalyst has a greater electronic density around the Fermi level than both the Co_9S_8 and $CoNi_2S_4$ models. These results indicate that the $Co_9S_8@CoNi_2S_4$ has the quickest charge transfer rate, as seen by the computed density of states (DOS) plot in Fig. 6b.

Furthermore, Fig. 6c illustrates the free energies of adsorption (ΔG_{H*}) for the various catalysts. The ΔG_{H*} value of the $Co_9S_8@CoNi_2S_4$ is 0.17 eV in the interface between Co_9S_8 and $CoNi_2S_4$, which is relatively close to the ideal ΔG_{H*} (0 eV), compared with the Co_9S_8 (1.03 eV) and $CoNi_2S_4$ (0.88 eV). The result suggests that the formed heterointerface between the Co_9S_8 and $CoNi_2S_4$ phases reduces the free energy of hydrogen adsorption, resulting in superior electrocatalytic process. The water adsorption energy is the critical factor for validating these catalysts' theoretical activity. Fig. S22 shows the optimized structure models for water adsorption, and the adsorption energies of the Co_9S_8, $CoNi_2S_4$ and $Co_9S_8@CoNi_2S_4$ structures are −0.33, −0.43, and −0.94 eV, respectively, as illustrated in Fig. 6d. This result demonstrates that the multidimensional $Co_9S_8@CoNi_2S_4$ heterojunction structure can offer abundant reactive sites, promote the

adsorption of active species, and form the catalyst-H_2O initial state more easily, which can accelerate the rapidly mass transfer and electron transfer during the catalytic process.

In addition, DFT was used to investigate the intricacies of the OER mechanism for catalysts. The intermediate structure models of OER for Co_9S_8, $CoNi_2S_4$ and $Co_9S_8@CoNi_2S_4$ are displayed in Figs S23, S24 and Fig. 6e. The rate-limiting step from *O to *OOH discloses a larger ladder span for Co_9S_8 and $CoNi_2S_4$ with the energy barrier of 0.72 and 0.86 eV, respectively, revealed in Fig. 6f. Clearly, the rate-limiting step of the $Co_9S_8@CoNi_2S_4$ catalyst is also the third electron transfer intermediate and the energy barrier value is about 0.59 eV on the heterogeneous interface between Co_9S_8 and $CoNi_2S_4$. The above results suggest that the energy barrier value of the $Co_9S_8@CoNi_2S_4$ is lower than that of the Co_9S_8 and $CoNi_2S_4$ catalysts. As the heterojunction interface optimizes the adsorption of various intermediates and accelerates water splitting kinetics, the DFT results reveal that the $Co_9S_8@CoNi_2S_4$ exhibits excellent water splitting capability. The theoretical calculation findings are consistent with the experimental data.

CONCLUSIONS
In summary, a straightforward hydrothermal, room-temperature growth and sulfurization process was used to effectively fabricate an integrated 1D, 2D, and 3D $Co_9S_8@CoNi_2S_4/NF$ multi-dimensional heterostructure. The heterostructure has well performed as the highly efficient bifunctional electrocatalyst for improved overall water splitting, which was confirmed by the excellent electrocatalytic activity toward both HER and OER with low overpotentials of only 68 and 170 mV at 10 mA cm^{-2}, respectively. The catalyst only needed a cell voltage of 1.49 V as both anode and cathode to achieve the current density of 10 mA cm^{-2} during the overall water splitting. The excellent
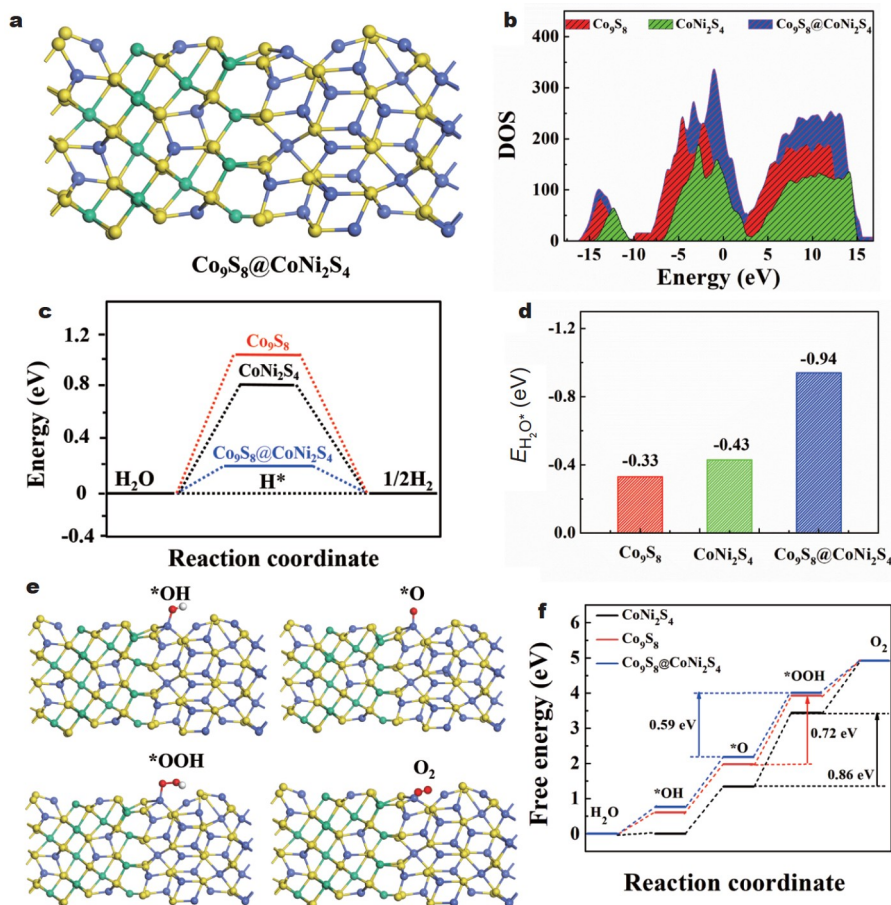
Figure 6 Mechanisms of the electrocatalytic activity revealed by *ab-initio* atomistic simulations. (a) The optimized $Co_9S_8@CoNi_2S_4$ model based on DFT calculations, (b) calculated DOS, (c) HER free-energy evolutions of different catalysts, (d) water adsorption energy values of different catalysts, (e) the intermediates' configurations of OER for the $Co_9S_8@CoNi_2S_4$ heterojunction, and (f) Gibbs free energy diagram for the four steps of the OER on Co_9S_8, $CoNi_2S_4$ and $Co_9S_8@CoNi_2S_4$ catalysts.

HER and OER bifunctional catalytic activity of $Co_9S_8@CoNi_2S_4$/NF can be attributed to the beneficial binding with H atoms in the heteromorphic $Co_9S_8@CoNi_2S_4$ interfaces, the integrated multidimensional structures, and low water adsorption energy, all of which contribute to optimizing the adsorption of multiple intermediates and facilitating water splitting kinetics, thereby improving electrocatalytic performance. This study advances our understanding of how to design multidimensional and heterostructured metallic sulfide electrocatalysts with increased HER and OER activity. Finally, the method of rational interface design provided in this study may be used to a variety of energy conversion and storage systems.

1   Ren JT, Wang YS, Chen L, *et al.* Binary FeNi phosphides dispersed on N,P-doped carbon nanosheets for highly efficient overall water splitting and rechargeable Zn-air batteries. Chem Eng J, 2020, 389: 124408

2   Wang HY, Weng CC, Ren JT, *et al.* An overview and recent advances in electrocatalysts for direct seawater splitting. Front Chem Sci Eng, 2021, 15: 1408–1426

3   Hou J, Wu Y, Zhang B, *et al.* Rational design of nanoarray architectures for electrocatalytic water splitting. Adv Funct Mater, 2019, 29: 1808367–1808405

4   Gao WK, Yang M, Chi JQ, *et al. In situ* construction of surface defects

of carbon-doped ternary cobalt-nickel-iron phosphide nanocubes for efficient overall water splitting. Sci China Mater, 2019, 62: 1285–1296

5   Ren JT, Yao Y, Yuan ZY. Fabrication strategies of porous precious-metal-free bifunctional electrocatalysts for overall water splitting: Recent advances. Green Energy Environ, 2021, 6: 620–643

6   Lu SS, Zhang LM, Dong YW, *et al.* Tungsten-doped Ni-Co phosphides with multiple catalytic sites as efficient electrocatalysts for overall water splitting. J Mater Chem A, 2019, 7: 16859–16866

7   Li Y, Tan X, Hocking RK, *et al.* Implanting Ni-O-VO_x sites into Cu-doped Ni for low-overpotential alkaline hydrogen evolution. Nat Commun, 2020, 11: 2720

8   Xu SS, Lv XW, Zhao YM, *et al.* Engineering morphologies of cobalt oxide/phosphate-carbon nanohybrids for high-efficiency electrochemical water oxidation and reduction. J Energy Chem, 2021, 52: 139–146

9   Chen W, Zhu X, Zhang Y, *et al.* Bimetal-organic frameworks from *in situ*-activated NiFe foam for highly efficient water splitting. ACS Sustain Chem Eng, 2021, 9: 1826–1836

10 Zheng X, Cui P, Qian Y, *et al.* Multifunctional active-center-transferable platinum/lithium cobalt oxide heterostructured electrocatalysts towards superior water splitting. Angew Chem Int Ed, 2020, 59: 14533–14540

11 Wang Y, Yan D, El Hankari S, *et al.* Recent progress on layered double hydroxides and their derivatives for electrocatalytic water splitting. Adv Sci, 2018, 5: 1800064–1800096

12 Liu H, Zhu J, Li Z, *et al.* Fe_2O_3/N doped rGO anode hybridized with NiCo LDH/$Co(OH)_2$ cathode for battery-like supercapacitor. Chem Eng J, 2021, 403: 126325

13 Wang F, He P, Li Y, *et al.* Interface engineered W$_x$C@WS$_2$ nanostructure for enhanced hydrogen evolution catalysis. Adv Funct Mater, 2017, 27: 1605802–1605808

14 Liu H, Ma X, Rao Y, *et al.* Heteromorphic NiCo$_2$S$_4$/Ni$_3$S$_2$/Ni foam as a self-standing electrode for hydrogen evolution reaction in alkaline solution. ACS Appl Mater Interfaces, 2018, 10: 10890–10897

15 Zhao L, Jia J, Yang Z, *et al.* One-step synthesis of CdS nanoparticles/MoS$_2$ nanosheets heterostructure on porous molybdenum sheet for enhanced photocatalytic H$_2$ evolution. Appl Catal B-Environ, 2017, 210: 290–296

16 Wu Y, Liu X, Han D, *et al.* Electron density modulation of NiCo$_2$S$_4$ nanowires by nitrogen incorporation for highly efficient hydrogen evolution catalysis. Nat Commun, 2018, 9: 1425

17 Wang B, Chen Y, Wang X, *et al.* rGO wrapped trimetallic sulfide nanowires as an efficient bifunctional catalyst for electrocatalytic oxygen evolution and photocatalytic organic degradation. J Mater Chem A, 2020, 8: 13558–13571

18 Zhao Y, Mavrokefalos CK, Zhang P, *et al.* Self-templating strategies for transition metal sulfide nanoboxes as robust bifunctional electrocatalysts. Chem Mater, 2020, 32: 1371–1383

19 Tian WW, Ren JT, Lv XW, *et al. In situ* sulfidation for controllable heterointerface of cobalt oxides-cobalt sulfides on 3D porous carbon realizing efficient rechargeable liquid-/solid-state Zn-air batteries. ACS Sustain Chem Eng, 2021, 9: 510–520

20 Jin L, Xu H, Wang C, *et al.* Multi-dimensional collaboration promotes the catalytic performance of 1D MoO$_3$ nanorods decorated with 2D NiS nanosheets for efficient water splitting. Nanoscale, 2020, 12: 21850–21856

21 Wang P, Qi J, Li C, *et al.* Hierarchical CoNi$_2$S$_4$@NiMn-layered double hydroxide heterostructure nanoarrays on superhydrophilic carbon cloth for enhanced overall water splitting. Electrochim Acta, 2020, 345: 136247

22 An T, Wang Y, Tang J, *et al.* Interlaced NiS$_2$-MoS$_2$ nanoflake-nanowires as efficient hydrogen evolution electrocatalysts in basic solutions. J Mater Chem A, 2016, 4: 13439–13443

23 Zhang X, Jin M, Lian Q, *et al.* Ion modification of transition cobalt oxide by soaking strategy for enhanced water splitting. Chem Eng J, 2021, 423: 130218

24 Han S, Chen Y, Hao Y, *et al.* Multi-dimensional hierarchical CoS$_2$@MXene as trifunctional electrocatalysts for zinc-air batteries and overall water splitting. Sci China Mater, 2021, 64: 1127–1138

25 Jing C, Guo X, Xia L, *et al.* Morphologically confined hybridization of tiny CoNi$_2$S$_4$ nanosheets into S, P co-doped graphene leading to enhanced pseudocapacitance and rate capability. Chem Eng J, 2020, 379: 122305

26 Hou T, Jia Z, Wang B, *et al.* MXene-based accordion 2D hybrid structure with Co$_9$S$_8$/C/Ti$_3$C$_2$T$_x$ as efficient electromagnetic wave absorber. Chem Eng J, 2021, 414: 128875

27 Jia H, Wang Z, Zheng X, *et al.* Interlaced Ni-Co LDH nanosheets wrapped Co$_9$S$_8$ nanotube with hierarchical structure toward high performance supercapacitors. Chem Eng J, 2018, 351: 348–355

28 Zhu H, Jiang R, Chen X, *et al.* 3D nickel-cobalt diselenide nanonetwork for highly efficient oxygen evolution. Sci Bull, 2017, 62: 1373–1379

29 Zou Z, Wang X, Huang J, *et al.* An Fe-doped nickel selenide nanorod/nanosheet hierarchical array for efficient overall water splitting. J Mater Chem A, 2019, 7: 2233–2241

30 Wang ZJ, Li MX, Yu JH, *et al.* Low-iridium-content IrNiTa metallic glass films as intrinsically active catalysts for hydrogen evolution reaction. Adv Mater, 2020, 32: 1906384

31 Dong B, Xie JY, Wang N, *et al.* Zinc ion induced three-dimensional Co$_9$S$_8$ nano-neuron network for efficient hydrogen evolution. Renew Energy, 2020, 157: 415–423

32 Qin JF, Yang M, Chen TS, *et al.* Ternary metal sulfides MoCoNiS derived from metal organic frameworks for efficient oxygen evolution. Int J Hydrogen Energy, 2020, 45: 2745–2753

33 Qu S, Huang J, Yu J, *et al.* Ni$_3$S$_2$ nanosheet flowers decorated with CdS quantum dots as a highly active electrocatalysis electrode for synergistic water splitting. ACS Appl Mater Interfaces, 2017, 9: 29660–29668

34 Zhang Q, Chen W, Chen G, *et al.* Bi-metallic nitroxide nanodot-decorated tri-metallic sulphide nanosheets by on-electrode plasma-hydrothermal sprouting for overall water splitting. Appl Catal B-Environ, 2020, 261: 118254

35 Qu S, Chen W, Yu J, *et al.* Cross-linked trimetallic nanopetals for electrocatalytic water splitting. J Power Sources, 2018, 390: 224–233

36 Liu T, Asiri AM, Sun X. Electrodeposited Co-doped NiSe$_2$ nanoparticles film: A good electrocatalyst for efficient water splitting. Nanoscale, 2016, 8: 3911–3915

37 Cai Z, Wu A, Yan H, *et al.* Hierarchical whisker-on-sheet NiCoP with adjustable surface structure for efficient hydrogen evolution reaction. Nanoscale, 2018, 10: 7619–7629

38 Lin Y, Pan Y, Liu S, *et al.* Construction of multi-dimensional core/shell Ni/NiCoP nano-heterojunction for efficient electrocatalytic water splitting. Appl Catal B-Environ, 2019, 259: 118039

39 Wen S, Chen G, Chen W, *et al.* Nb-doped layered FeNi phosphide nanosheets for highly efficient overall water splitting under high current densities. J Mater Chem A, 2021, 9: 9918–9926

40 Hou J, Sun Y, Cao S, *et al.* Graphene dots embedded phosphide nanosheet-assembled tubular arrays for efficient and stable overall water splitting. ACS Appl Mater Interfaces, 2017, 9: 24600–24607

41 Yu L, Zhou H, Sun J, *et al.* Cu nanowires shelled with NiFe layered double hydroxide nanosheets as bifunctional electrocatalysts for overall water splitting. Energy Environ Sci, 2017, 10: 1820–1827

42 Wang JG, Hua W, Li M, *et al.* Structurally engineered hyperbranched NiCoP arrays with superior electrocatalytic activities toward highly efficient overall water splitting. ACS Appl Mater Interfaces, 2018, 10: 41237–41245

43 Chen W, Zhang Y, Huang R, *et al.* Ni-Co hydroxide nanosheets on plasma-reduced Co-based metal-organic nanocages for electrocatalytic water oxidation. J Mater Chem A, 2019, 7: 4950–4959

44 Zhang Q, Chen W, Chen G, *et al.* Trimetallic octahedral Ni-Co-W phosphoxide sprouted from plasma-defect-engineered Ni-Co support for ultrahigh-performance electrocatalytic hydrogen evolution. ACS Sustain Chem Eng, 2021, 9: 7454–7465

45 Wang C, Zhu M, Cao Z, *et al.* Heterogeneous bimetallic sulfides based seawater electrolysis towards stable industrial-level large current density. Appl Catal B-Environ, 2021, 291: 120071

Author contributions Chen W designed and engineered the samples; Chen W analyzed the data and wrote the paper with the support from Zang SQ; Hu Y conducted the theoretical simulation; Cui J and Wang J performed the experiments; Ostrikov K and Peng P helped to revise and polish the paper; Wei W and Zhang Y helped to conduct some characterizations. All authors contributed to the general discussion.

Conflict of interest The authors declare that they have no conflict of interest.

Supplementary information Supporting data are available in the online version of the paper.

Shuang-Quan Zang received his PhD degree in chemistry from Nanjing University in 2006 under the supervision of Prof. Qingjin Meng. After postdoctoral research with Prof. Thomas C. W. Mak at The Chinese University of Hong Kong, he joined the College of Chemistry, Zhengzhou University. He received the National Science Fund for Distinguished Young Scholars in 2018. He is serving as the Dean of the College of Chemistry and Green Catalysis Center, Zhengzhou University. His current scientific interests focus on atomically-precise metal clusters, cluster-assembled materials, and functional metal-organic frameworks.

多维镍钴硫化物异质结电催化剂用于高效全水解

陈稳霞[1], 胡应杰[1,3], 彭鹏[2], 崔金海[1], 王军梅[1], 魏伟[1], 张永亚[1], 欧思聪[4], 臧双全[2*]

摘要 异质结构工程在高效全解水催化剂方面具有突出的应用前景. 然而, 生产廉价高效的双功能电催化剂仍然是一个巨大的挑战. 因此, 我们受构树启发, 通过一种简单的方法在泡沫镍基体上合成了高催化活性和稳定性的$Co_9S_8@CoNi_2S_4$/NF异质结. 该过程包括NiCo层状双氢氧化物在泡沫镍基体上的原位生长和原位衍生ZIF-67, 并伴随S原子掺杂. 所获得的$Co_9S_8@CoNi_2S_4$/NF多维度异质结包括一维纳米线、二维纳米片和纳米颗粒. 优化的$Co_9S_8@CoNi_2S_4$/NF中硫含量为10%, 在1.0 mol L^{-1} KOH溶液中, 电流密度为10 mA cm^{-2}时, 具有优异的电催化活性, 其析氢和析氧过电位分别为68和170 mV, 优于最近报道的过渡金属基电催化剂. 该催化剂优异的催化性能主要归因于$CoNi_2S_4$与Co_9S_8之间较强的界面耦合、多维结构以及定制电子结构优势. 密度泛函理论表明, Co_9S_8和$CoNi_2S_4$之间的界面优化了多个中间体的吸附, 进一步促进了水裂解动力学. 本工作为高效异质结构工程催化体系的设计提供了一种通用的方法.